EPJ AP
Applied Physics
www.epj.org

Eur. Phys. J. Appl. Phys. **43**, 1–18 (2008) DOI: 10.1051/epjap:2008143

Resonant terahertz transmission in plasmonic arrays of subwavelength holes

W. Zhang

Eur. Phys. J. Appl. Phys. **43**, 1–18 (2008)
DOI: 10.1051/epjap:2008143

**The European
Physical Journal
Applied Physics**

Resonant terahertz transmission in plasmonic arrays of subwavelength holes

W. Zhang[a]

School of Electrical and Computer Engineering, Oklahoma State University, Stillwater, 74078 Oklahoma, USA

Received: 1st May 2008 / Accepted: 17 June 2008

Abstract. A review of transmission properties of two-dimensional plasmonic structures in the terahertz regime is presented. Resonant terahertz transmission was demonstrated in arrays of subwavelength holes patterned on both metals and semiconductors. The effects of hole shape, hole dimensions, dielectric function of metals, array film thickness, and a dielectric overlayer were investigated by the state-of-the-art terahertz spectroscopy modalities. Extraordinary terahertz transmission was demonstrated in arrays of subwavelength holes made even from Pb, a generally poor metal, and having optically thin thicknesses less than one-third of a skin depth. We also observed a direct transition of a surface plasmon resonance from a photonic crystal minimum in a photo-doped semiconductor array. According to the Fano model, transmission properties of such plasmonic arrays are characterized by two essential contributions: resonant excitation of surface plasmons and nonresonant direct transmission. Plasmonic structures will find fascinating applications in terahertz imaging, biomedical sensing, subwavelength terahertz spectroscopy, and integrated terahertz devices.

PACS. 73.20.Mf Collective excitations (including excitons, polarons, plasmons and other charge-density excitations) – 78.47.+p Time-resolved optical spectroscopies and other ultrafast optical measurements in condensed matter – 42.79.Ag Apertures, collimators

1 Introduction

Two-dimensional (2D) array of subwavelength holes, which enables extraordinary transmission of electromagnetic waves, has become a unique component in integrated nano- and micro-photonics and may find breakthrough applications in semiconductor nanofabrication, microscopy, display technology, and bio-chemical sensing [1–3]. Understanding the physical origin of resonant properties in such plasmonic structures has attracted significant interest in a broad spectrum of electromagnetic waves. Surface plasmons (SPs) are collective excitations for quantized oscillations of electrons [4]. The resonant interaction between electron-charged oscillations near the surface of metal and the electromagnetic field creates SPs and results in rather unique properties [5]. Recent advance in extraordinary transmission of light has demonstrated when light passed through periodic subwavelength holes perforated in a metallic film, the resulted higher-than-unity transmission was primarily attributed to resonant excitation of SPs [1,3]. Light was coupled into the holes in the form of SPs which were squeezed through the holes and then converted back into light on the far side of the holes. Extensive experimental and theoretical studies have been carried out to approach fundamental understanding of this extraordinary transmission and to explore its potential applications in a broad range of disciplines [6–9].

In the terahertz regime, SPs have recently attracted much attention and become an attractive new area [10–19]. Due to a drastic increase in the value of dielectric function $\varepsilon_m = \varepsilon_{rm} + i\varepsilon_{im}$, most metals become highly conductive at terahertz frequencies. This has resulted in discrepancies in SP-enhanced transmission of terahertz radiation with that in the visible spectral regime. Experimental results on transmission properties of light in metallic structures have indicated that SP-enhanced transmission is normally achieved in metals with large ratio of the real to the imaginary dielectric constant, $-\varepsilon_{rm}/\varepsilon_{im} \gg 1$ [20,21]. In the terahertz regime, however, this ratio becomes $-\varepsilon_{rm}/\varepsilon_{im} < 1$ for non-transition metals, such as Ag, Au, Cu, and Al [22]. This was considered as a limitation to realize resonant excitation of terahertz SPs in the periodic subwavelength structures. The recent studies, however, have demonstrated that an appropriate surface corrugation provided by the subwavelength structures could facilitate the resonant excitation of SPs even with $-\varepsilon_{rm}/\varepsilon_{im} < 1$ [23]. SP-enhanced terahertz transmission has been experimentally observed in subwavelength hole arrays patterned in metal films made from both good and generally poor metals [24,25].

---

[a] e-mail: `weili.zhang@okstate.edu`

In addition to metals, semiconductors with high density of free carriers exhibit metallic properties by having a negative real part of dielectric function ($\varepsilon_{rm} < 0$), and thus can be used as alternate metallic media to support SPs at terahertz frequencies. As a result, enhanced terahertz transmission was demonstrated in microstructured hole arrays made from both intrinsically doped and photo-doped semiconductors [11,26–30]. The advantage of semiconductors is that their dielectric function can be modified by varying doping concentration, temperature, or optical excitation. This in turn enables tuning and switching of SPs. Such semiconductor plasmonic arrays may find applications in all solid state terahertz optoelectronic devices, such as high-throughput, high resolution filters, and focusing elements for terahertz imaging system.

The combination of SPs and terahertz spectroscopy will be a fruitful field both in fundamental understanding the properties of terahertz SPs and their promising applications. In this article, we present our recent work on resonant terahertz transmission in lithographically fabricated 2D metal and semiconductor arrays of subwavelength holes. The presentation is organized as follows: in Section 2, we describe experimental methods employed in these studies, including terahertz time-domain spectroscopy and optical pump-terahertz probe spectroscopy. In Section 3, the lithographic fabrication processes of the plasmonic arrays are presented. In Section 4, we review resonant terahertz transmission in metal arrays of subwavelength holes. The interesting properties of plasmonic structures made from semiconductors are introduced in Section 5. Finally, a conclusion is drawn in Section 6.

2 Experimental methods

2.1 Terahertz time-domain spectroscopy

Broad-band photoconductive switch-based terahertz time-domain spectroscopy (THz-TDS) transmission measurements were employed to study resonant properties of the 2D intrinsic plasmonic arrays [31]. As illustrated in Figure 1, the THz-TDS system was comprised of a GaAs photoconductive transmitter, a silicon-on-sapphire (SOS) photoconductive receiver, and four parabolic mirrors, aligned in an 8-F confocal geometry [32]. A self-mode-locked Ti:sapphire laser capable of generating 88-MHz, 800-nm, and 26-fs ultrafast optical pulses was used to gate the photoconductive switches, with 10-mW average power on each side. The terahertz beam emitted from the transmitter was spatially gathered by a silicon lens and then collimated into a parallel beam by the parabolic mirror, M_1. In order to characterize the array samples of small dimensions, the terahertz beam was compressed by an additional pair of $f = 50$ mm parabolic mirrors, M_2 and M_3, located midway between the two primary parabolic mirrors, M_1 and M_4. The beam was then focused into another silicon lens at the receiver end by M_4. This 8-F confocal system not only ensured an excellent beam coupling between the transmitter and receiver but also compressed the terahertz beam to a frequency independent diameter of 3.5 mm. Figure 2 shows a measured terahertz pulse and the corresponding Fourier-transformed spectrum. As can be seen that the THz-TDS system has a useful bandwidth of 0.1 to 4.5 THz (3 mm–67 μm) and a signal-to-noise ratio (S/N) of >15 000:1.

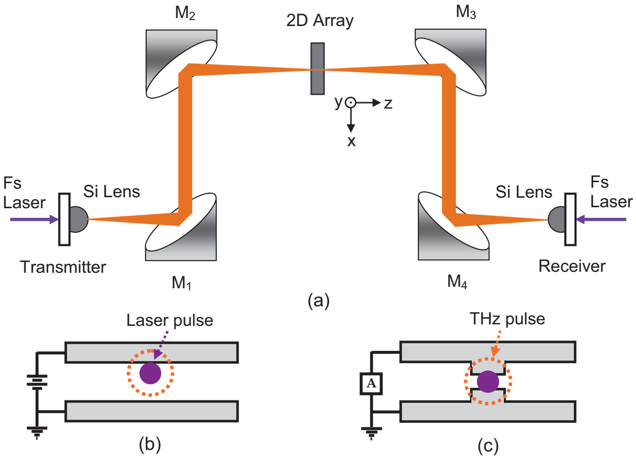

Fig. 1. (Color online) Schematic diagram of the terahertz time-domain spectroscopy system: (a) the 8F confocal system; (b) GaAs transmitter; (c) silicon on sapphire receiver.

In the transmission measurements, the array was placed midway between the parabolic mirrors, M_2 and M_3, at the waist of the terahertz beam. The terahertz radiation penetrated the array at normal incidence with a P-polarized electric field. A blank slab identical to the array substrate was used as a reference. The transmitted electric field of the terahertz pulses through the sample and reference were recorded in time domain and then Fourier-transformed into frequency-domain amplitude spectra as $E_a(\omega)$ and $E_r(\omega)$, respectively. Due to limited thickness of the arrays, the main transmitted terahertz pulse was trailed by multiple-reflected pulses in time domain. However, the clean separation between the main transmitted pulse and the first internal reflection enabled data analysis on the main transmitted pulse only. In order to further increase the S/N in the measurements, each curve was an average of a number of individual scans. The absolute amplitude transmission of the array was defined as $|\tilde{t}(\omega)| = |E_a(\omega)/E_r(\omega)|$ and the corresponding phase change was obtained through the relation, $\phi(\omega) = \arg[\tilde{t}(\omega)]$ [10].

2.2 Optical pump-terahertz probe spectroscopy

Optical pump-terahertz probe characterization was used to investigate resonant properties of the non-intrinsic plasmonic arrays of subwavelength holes, such as the photo-doped semiconductor samples [29,33]. The terahertz pulses were generated from a 2 mm-thick ZnTe crystals by optical rectification and were detected by use of electro-optical sampling in a 1-mm-thick ZnTe crystal [34]. A femtosecond regenerative Ti:sapphire amplifier (Hurricane, Spectra-Physics), capable of generating 750-mW,

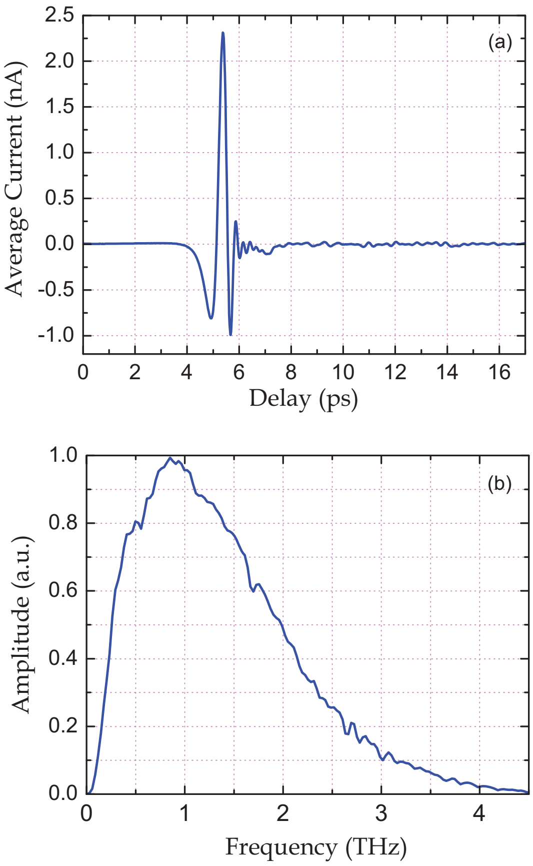

Fig. 2. (Color online) (a) Time-domain terahertz pulse and (b) corresponding Fourier transformed spectrum recorded in the terahertz spectroscopy system shown in Figure 1.

100-fs intense laser pulses at a repetitions rate of 1 kHz, was used as the optical source for terahertz pulse generation, detection, and photo-doping of the semiconductor arrays. The generated terahertz pulses were guided towards the detector by four parabolic mirrors in a confocal geometry. The terahertz focal spot size between the two inner parabolic mirrors was 0.74 mm. A schematic diagram of the experimental approach is illustrated in Figure 3. The array sample was placed at 3 mm before the focal spot, where the terahertz beam diameter was approximately 1.50 mm. The optical excitation beam had a larger size in diameter and overlapped well with the terahertz spot on the sample.

3 Sample fabrications

In this investigation, we have fabricated two types of plasmonic arrays by use of conventional photolithography and thermal metallization processing. The type-I arrays were array-on-silicon samples with a patterned metal film evaporated on blank silicon substrates, while the type-II arrays were freestanding structures with subwavelength holes etched through thin silicon slabs of 30–50 μm thickness [10,27].

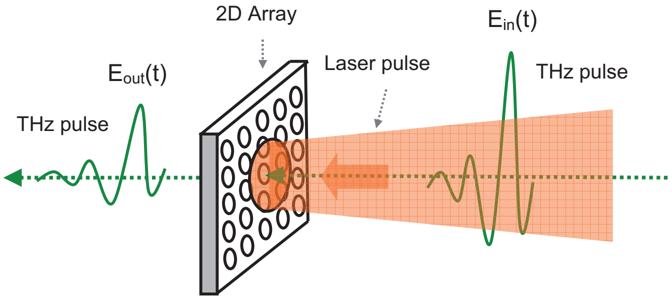

Fig. 3. (Color online) Schematic diagram of the optical pump-terahertz probe spectroscopy.

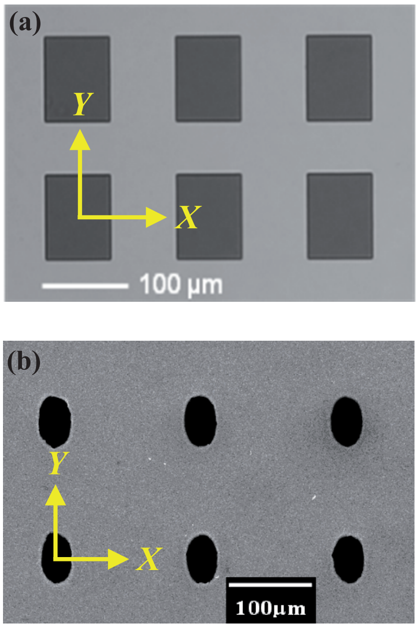

Fig. 4. (Color online) Images of plasmonic arrays of subwavelength holes: (a) microscopic image of the metal array on silicon; (b) SEM image of the free standing array.

The array-on-silicon samples were lithographically fabricated on high quality silicon wafers (0.64-mm-thick, p-type resistivity $\rho = 20\ \Omega\,\mathrm{cm}$). The photolithography processing included spin application of photoresist adhesive promoter (HMDS, Microchem), spin coating of positive photoresist (S-1813, Shirpley), convection oven bakes, contact mode exposure, and resist development (2401 developer, Microchem). The patterned wafer was then thermally evaporated (BOC-306) with a layer of metal films, such as Al, Ag, and Pb. A follow up process was acetone lift-off to reveal the metal patterns of subwavelength hole arrays [25]. A high resolution optical image of a square array of 100 μm $\times$ 80 μm rectangular holes of a periodicity of 160 μm is illustrated in Figure 4a.

The freestanding arrays were fabricated from 30–50 μm-thick silicon wafers. The fabrication processes have included conventional photolithography and reactive ion etching (RIE) processes. The wafer was first spin-coated with SU-8 2025 photoresist (Microchem) and exposed with a UV light source while under the mask [27]. After development, the RIE process has created through-holes on the bare silicon while the rest of the area of the wafer was still protected with photoresist. A mixed gas flow of 12.5-sccm SF_6 and 1.5-sccm O_2 driven under a RF power of 400 W delivered an etching rate of 5 μm/min for silicon. Figure 4b shows a scanning electron microscopic (SEM) image of a freestanding array of elliptical holes with a periodicity of 160 μm and dimensions of 75 μm along the major axis (y) and 45 μm along the minor axis (x).

4 Resonant enhancement of terahertz transmission in metal arrays

In this section, we present our recent work on resonant terahertz transmission in both optically thick and optically thin 2D metal arrays of subwavelength holes. At the primary SP $[\pm 1, 0]$ mode, amplitude transmission efficiency of up to nine tenths of the maximum resonant transmission was achieved when the array thickness was only one third of the skin depth [10,24]. By use of highly reproducible subwavelength arrays we have demonstrated the effect of dielectric function of metals on transmission properties of terahertz radiation [25]. We have also shown that the enhanced terahertz transmission in the 2D arrays of subwavelength holes is resulted from contributions of both SPs and nonresonant transmission [35]. Finally, we present the influence of a dielectric thin film on resonant terahertz transmission in a plasmonic array of subwavelength holes of asymmetric dielectric-metal interfaces [36].

4.1 Resonant excitation of terahertz SPs in optically thick metal arrays

Optically thick metallic films patterned with subwavelength hole arrays have been of great interest in studies of plasmonic transmission properties in a broad range of electromagnetic spectrum. In the terahertz regime, THz-TDS measurements have revealed enhanced amplitude transmission and a sharp phase peak in 2D optically thick arrays of metal holes [10]. Correspondingly, the measured transmission magnitude has the shape of the derivative of this peak, which is consistent with the Kramers–Kronig relations. In addition, we found that the hole shape of the thin metallic films had a significant effect on the transmission magnitude and the corresponding phase change of the terahertz radiation.

Each array was a lithographically fabricated 520-nm-thick aluminum film deposited on silicon substrate. To investigate the hole shape effect, two array samples were prepared. Sample A is a square array of 80 μm (x axis) $\times$ 100 μm (y axis) rectangular holes as shown in Figure 4a, while sample B is a square array of 100-μm-diameter circular holes. The periodicity of these arrays is $L = 160$ μm in both 2D directions. Figures 5a and 5b illustrate the transmitted terahertz pulses and the corresponding amplitude spectra of the reference and the samples.

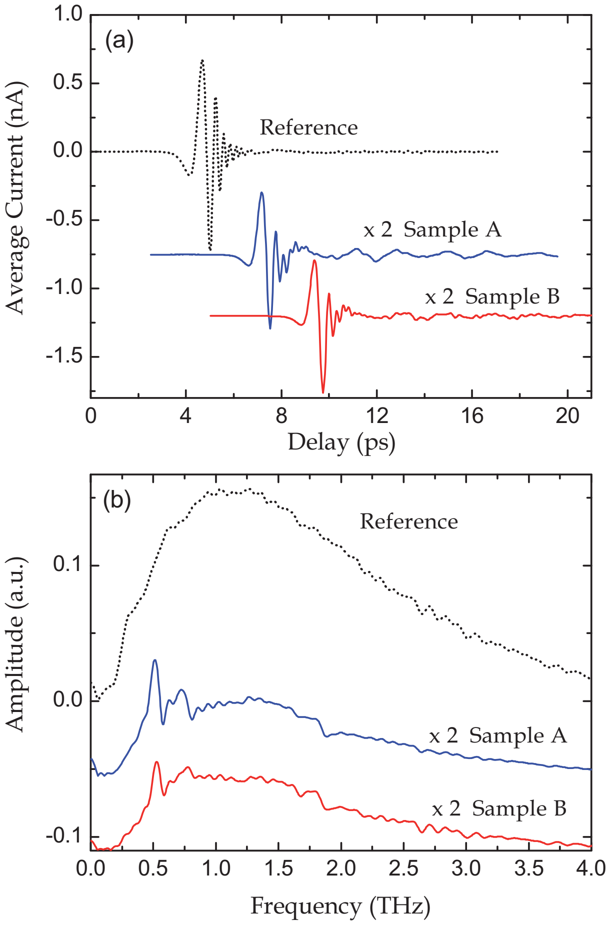

Fig. 5. (Color online) (a) Measured transmitted terahertz pulses and (b) the corresponding spectra through the reference and samples (multiplied by 2×). The curves in (a) and (b) are vertically displaced for clarity.

The extracted amplitude transmission and the corresponding phase change are shown in Figures 6a and 6b, respectively. Several well-defined resonant features were observed and essentially attributed to resonant excitation of SPs at terahertz frequencies. In particular, the sharp resonance near 0.5 THz exhibits 2.26 and 1.45 power transmission efficiency for samples A and B, respectively, when normalized to the area occupied by the holes, as referred to as higher-than-unity extraordinary transmission [1].

In a metal array, SPs can be resonantly excited at the metal-dielectric interfaces following momentum conservation [4,37,38],

$$\mathbf{k}_{sp} = \mathbf{k}_{||} + \mathbf{G}_{mn} \tag{1}$$

where $\mathbf{k}_{sp}$ is the wave vector of SPs, $\mathbf{k}_{||}$ is the in-plane wave vector, $\mathbf{G}_{mn}$ is the reciprocal lattice vectors, m and n are integers of the SP modes. In the 2D array of subwavelength holes, the resonant frequencies of SPs at the metal-dielectric interface can be described through the dispersion relation at normal incidence as [4,37,38],

$$\omega_{sp}^{m,n} = c\,\mathbf{G}_{mn}\left(\frac{\varepsilon_d \varepsilon_m}{\varepsilon_d + \varepsilon_m}\right)^{-1/2}, \tag{2}$$

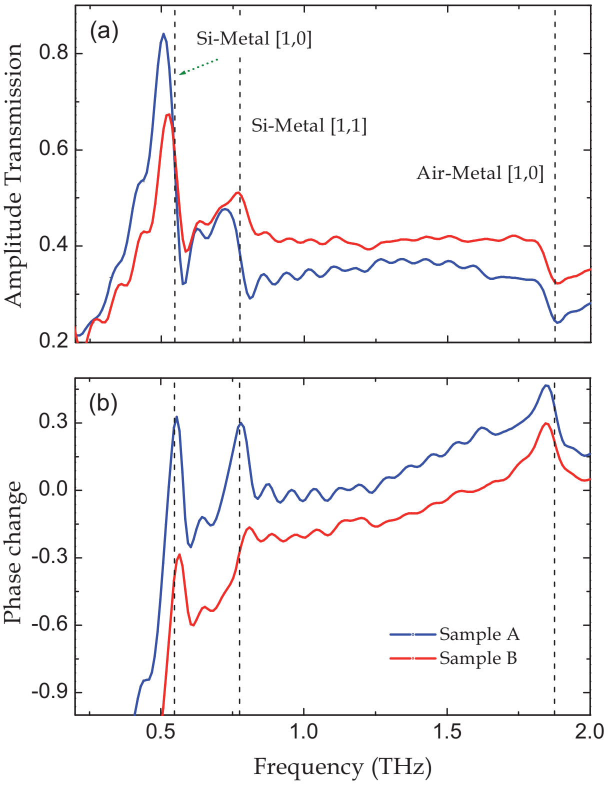

Fig. 6. (Color online) (a) Measured frequency-dependent amplitude transmission of the signal pulse compared to the reference pulse. (b) Corresponding comparative phase change in radians for Sample A, 80 μm × 100 μm rectangular hole arrays and Sample B, 100 μm diameter circular hole arrays. In (a), the spectrum of Sample B is lifted by 0.1 and in (b), the phase change of Sample B is lowed by 0.1 for clarification. The dashed lines indicate the SP resonance frequencies.

where ε_m and ε_d denote the dielectric function of metal and the adjacent dielectric medium, respectively, $\mathbf{G}_{mn} = (2\pi/L)(m^2+n^2)^{1/2}$ is the grating momentum wave vector for the 2D square hole arrays, L is the periodicity of the array, c is the speed of light in vacuum.

In the terahertz regime, the dielectric constant of metals is several orders higher than that of dielectric media. For example, $\varepsilon_m = -1.12\times10^5 + 1.45\times10^6 i$ for aluminum at 0.55 THz, while $\varepsilon_d = 11.68$ and $\varepsilon_d = 1$ for silicon and air, respectively. Thus, the SP modes excited in the array can be approximately given as [4,10,37–39]

$$\omega_{SP}^{m,n} \cong c\,\mathbf{G}_{mn}\,\varepsilon_d^{-1/2}. \tag{3}$$

The observed sharp phase peaks centered at the SP resonance modes are indicated by the vertical dashed lines: the metal-Si modes at 0.55 $[\pm1,0]$ and 0.78 $[\pm1,\pm1]$ THz; the metal-air mode $[\pm1,0]$ at 1.88 THz. Besides samples A and B, a set of arrays with rectangular, square, and circular holes has been measured. We observed that with the same fundamental period the hole shape and dimensions could appreciably modify the strengths and shapes of the transmission and the phase change peaks due to the polarization dependent coupling of SPs.

4.2 Evolution of terahertz SP resonance in optically thin metal arrays

Resonant excitation of SPs has been widely studied in optically thick 2D hole arrays in a broad spectral range. It is interesting, however, whether SPs can be excited in optically thin metallic arrays of sub-skin-depth thicknesses. Here, we demonstrate resonant terahertz transmission through subwavelength hole arrays patterned on metallic films with thicknesses less than a skin depth. Our experimental results have revealed a critical array thickness, above which the SP resonance begin to establish [24]. The maximum amplitude transmission was achieved when the thickness of metal film approaches a skin depth. However, enhanced terahertz transmission of up to nine tenths of the maximum transmission was realized at a film thickness comparable to the skin depth at wavelengths of light, only one third of the skin depth at the metal-silicon $[\pm1,0]$ SP mode, 0.55 THz.

We have processed a set of metallic arrays of subwavelength rectangular holes from Pb film deposited on the silicon wafer [24]. The rectangular holes have physical dimensions of 100 μm × 80 μm with a periodicity of 160 μm. Pb was chosen as the constituent metal of the arrays mainly because of two reasons. First, extraordinary terahertz transmission in Pb subwavelength hole arrays has been demonstrated with an amplitude efficiency of up to 82% at 0.55 THz, which is close to the performance of arrays made from good electrical conductors such as Ag, Al, and Au [22,25]. Second, the skin depth of Pb at 0.55 THz is 320 nm, nearly three times of those of Ag and Al. It thus provided a large dynamic range to characterize the evolution of SP resonance at sub-skin-depth thicknesses.

The value of skin depth of electromagnetic waves in metal is determined by the penetration distance at which the electric field falls to $1/e$. The SPs, which propagate along metal-dielectric interface, decay exponentially in both media. At terahertz frequencies, the complex wave vector inside the metal perpendicular to the interface is approximately given as [10,24,25]

$$k_z = \frac{\omega}{c}\varepsilon_m^{1/2}, \tag{4}$$

where ω is the angular frequency. Since only the imaginary part of k_z causes the exponential decay of electric fields, the skin depth can be is defined as [21,40]

$$\delta = \frac{1}{\mathrm{Im}\,(k_z)} = \frac{c}{\omega}\,\frac{1}{\mathrm{Im}\left(\varepsilon_m^{1/2}\right)} = \left(\frac{2}{\omega\mu_0\sigma_{dc}}\right)^{1/2} \tag{5}$$

where μ_0 is the vacuum permeability and σ_{dc} is the d.c. conductivity of metal. Based on this relation, frequency dependent skin depths of various metals are plotted in the terahertz regime in Figure 7. As can be seen, the skin depths for Pb, Al, and Ag at 0.55 THz, the primary SP $[\pm1,0]$ resonance, are estimated to be 320, 110, and 83 nm, respectively.

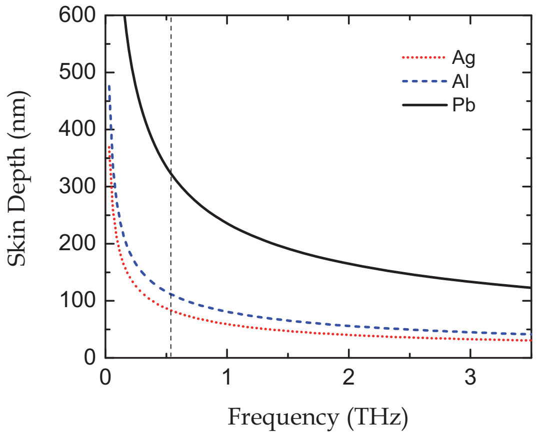

Fig. 7. (Color online) Frequency-dependent skin depth of Pb, Al, and Ag calculated from the published values of the dielectric constants (Ref. [22]). The vertical dotted line represents the $[\pm 1, 0]$ SP mode at 0.55 THz for the Pb-silicon interface.

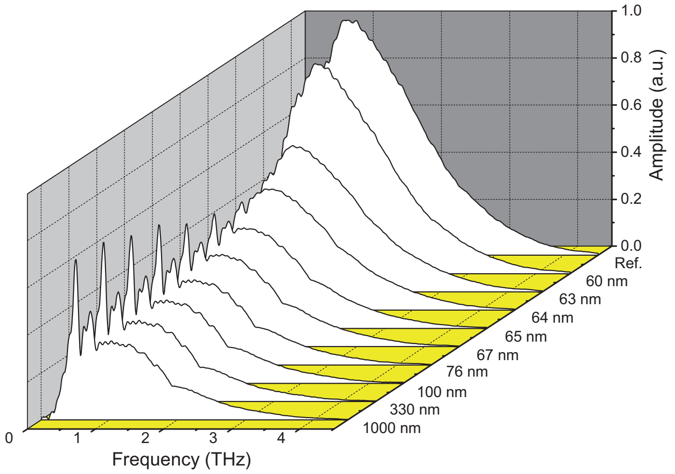

Fig. 8. (Color online) Fourier-transformed spectra of the transmitted terahertz pulses through reference and the subwavelength Pb hole arrays with different film thicknesses.

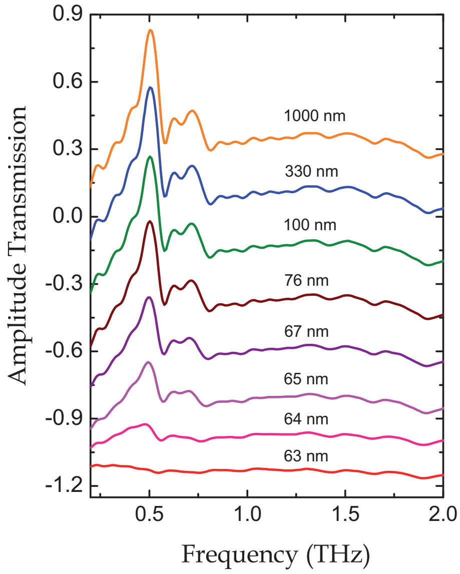

Fig. 9. (Color online) Measured amplitude transmission of the Pb arrays with different thicknesses. The curves are vertically displaced for clarity.

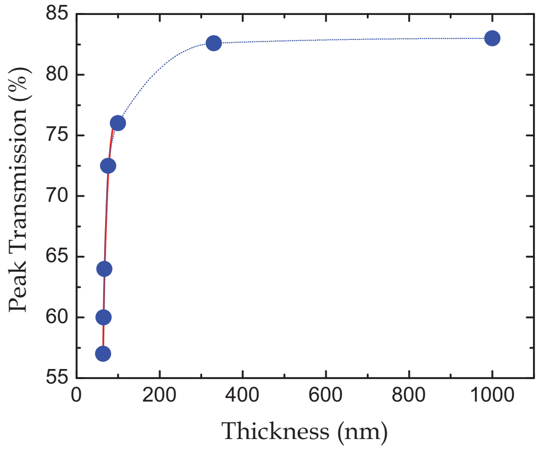

Fig. 10. (Color online) Measured peak amplitude of the $[\pm 1, 0]$ SP mode at 0.55 THz as a function of the Pb thickness (dots), connected by a dotted curve to guide the eye. The solid curve is an exponential fit for the region of array thicknesses below 100 nm.

Pb arrays with various thicknesses ranging from 60 to 1000 nm were prepared. In the THz-TDS measurements, the input terahertz radiation were polarized along the minor axes (80 μm) of the rectangular holes and penetrate the array at normal incidence. In Figure 8, evolution of the SP resonance as a function of the array film's thickness is depicted in the Fourier-transformed spectra of the reference and the samples. When the array film is thin, the spectrum showed no resonance but similar features of the reference spectrum with attenuation. At 64 nm, which was observed as a critical thickness for the Pb array, the SP resonance excited at the Pb-Si interface appeared in the spectrum. Above this critical thickness, the resonance peak is enhanced with thicker array film.

In Figure 9, evolution of SP resonance as a function of array film thickness is depicted in the amplitude transmission spectra of various arrays. It clearly reveals two regions of thickness dependence. Below the critical thickness, 64 nm, the frequency-dependent transmission is nearly flat, showing no resonance peak. Above the critical thickness, a resonance at 0.55 THz appears in the transmission, whose amplitude increases with array thickness while the background transmission is reduced in the mean time. This resonance is attributed to the excitation of SPs at the Pb-Si interface. Immediately above the critical thickness, the resonance amplitude is very sensitive to the thickness of arrays.

The dependence of peak transmission on array thickness above the critical thickness is shown in Figure 10. The amplitude transmission efficiency increases exponentially when the array thickness is below 100 nm. It then saturates gradually and approaches the maximum at one skin depth [24]. It is worth noting that a transmission efficiency as high as 76% was achieved at array thickness of 100 nm, only one third of skin depth. This value is more than nine tenths of the maximum transmission efficiency achieved at one skin depth. For comparison, we have fabricated two additional arrays of same structure but made from Ag and Al of one third of skin depth. The measured transmission efficiencies are all above nine tenths of their maximum amplitude transmission. This finding may extensively reduce the metal thickness of plasmonic components for applications in photonic, optoelectronic, and sensing devices.

4.3 Effect of dielectric function of metals on resonant terahertz transmission

The dielectric function of constituent metals was found to play an essential role in the extraordinary transmission of light in 2D subwavelength hole arrays. Owing to different ratio of the real to imaginary dielectric function, $-\varepsilon_{rm}/\varepsilon_{im}$, transmission properties of light showed a large difference in the arrays made from Ag, Au, and Cr [1,20,21]. The SP-enhanced transmission efficiency of light was increased with higher ratio $-\varepsilon_{rm}/\varepsilon_{im}$ [1,20,21], for example, the transmission efficiency of Ag arrays was several times higher than that of Ni arrays of the same structure [21]. At terahertz frequencies, however, the values of dielectric function of metals are several orders of magnitude higher than those at visible frequencies. The dielectric function of metals may influence the extraordinary terahertz transmission differently in subwavelength structures than that at visible frequencies.

To explore dielectric function related terahertz transmission properties of metal arrays at different resonance frequencies, two types of array samples were lithographically fabricated: array-on-silicon samples with patterned optically thick metal film on blank silicon substrate for the metal-silicon $[\pm 1, 0]$ mode at 0.55 THz [10,25] and free-standing metallic arrays for the metal-air $[\pm 1, 0]$ mode at 1.60 THz [25,27]. Our THz-TDS measurements have shown that the resonant terahertz transmission was increased with the higher ratio $-\varepsilon_{rm}/\varepsilon_{im}$ for metals with dielectric function following the Drude model. This result is consistent with the observation at optical frequencies [20,21]. However, due to significant increase in the values of dielectric function, the gap in the resonance peaks between arrays made from different metals was narrowed down extensively compared to the resonant transmission of light.

The dielectric function of the non-transition metals such as Ag, Al, and Pb can be well described by the Drude model [22], $\varepsilon_m(\omega) = \varepsilon_\infty - \omega_p^2/(\omega^2 + i\omega\Gamma)$, where $\omega_p/2\pi$ is the plasma frequency, $\Gamma/2\pi$ is the carrier damping frequency, and ε_∞ is the high frequency dielectric constant. Based on the experimentally determined parameters given in reference [22], Figure 11 shows the frequency-dependent complex dielectric function for various constituent metals in the frequency range of 0.1–3.0 THz. It can be seen that the absolute values of both the real and the imaginary parts of dielectric function are several orders of magnitude higher than that at visible frequencies.

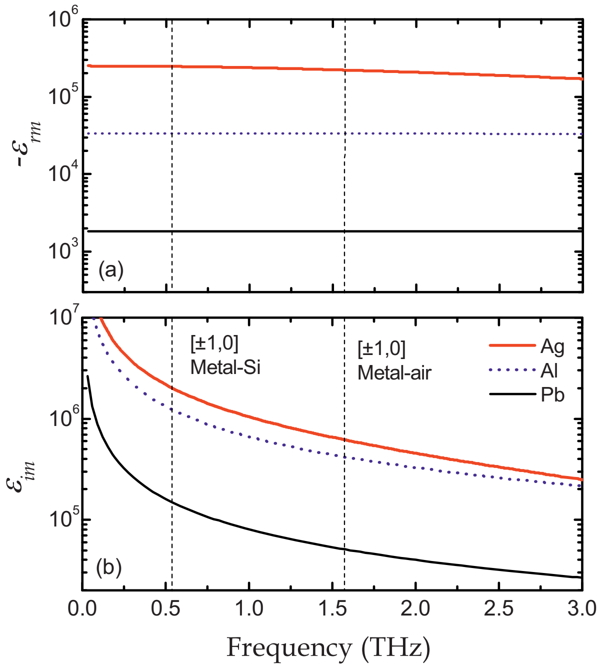

Fig. 11. (Color online) Frequency-dependent Drude model dielectric functions of Ag, Al, and Pb (Ref. [22]): (a) real dielectric function, $-\varepsilon_{rm}$; (b) imaginary dielectric function, ε_{im}. The vertical dashed lines indicate the observed $[\pm 1, 0]$ metal-Si SP mode at 0.55 THz and the $[\pm 1, 0]$ metal-air SP mode at 1.60 THz.

At 0.55 THz, the ratios $-\varepsilon_{rm}/\varepsilon_{im}$ for Ag, Al, and Pb are 0.12, 0.03, and 0.01, respectively, indicating that Ag is still a better metal than others, and was expected to show resonance with higher amplitude transmission [21]. Practically, as shown in Figure 12, the Ag array indeed showed the highest amplitude transmission 87%, while the Al and Pb arrays followed after with small attenuation, giving 85.5% and 82%, respectively. Even though the amplitude transmission of these arrays revealed small differences, it indeed increased with higher ratio $-\varepsilon_{rm}/\varepsilon_{im}$. This showed good consistency with those observed at visible frequencies [20,21]. Compared to excellent metals, Pb is generally considered as a poor electrical conductor. However, the drastic increase in dielectric constant enables Pb to behave as a better metal towards the establishment of SP-enhanced transmission at terahertz frequencies. In Figure 13, the measured peak transmission at the SP $[\pm 1, 0]$ resonance 1.60 THz for Ag, Al, and Pb are 82%, 81%, and 72.5%, respectively, showing similar properties as observed at the SP $[\pm 1, 0]$ metal-Si resonance 0.55 THz. The difference in amplitude transmission for arrays made from these metals was arisen from the difference in effective propagation length of SPs.

We have also fabricated array-on-silicon samples with various thicknesses to verify the experimental results. Figure 14 illustrates the peak transmittance measured at the 0.55 $[\pm 1, 0]$ THz SP mode for the Ag, Al, and Pb

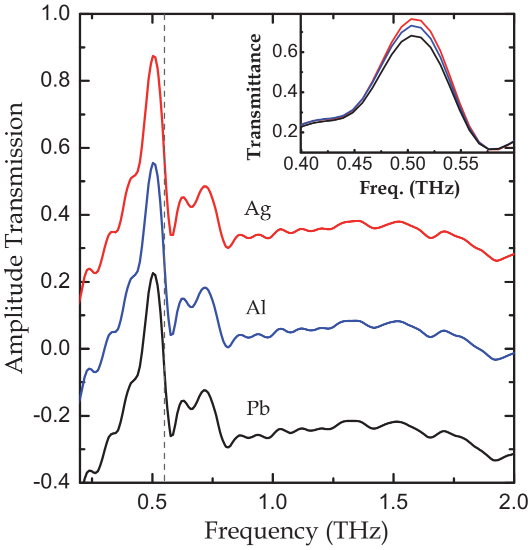

Fig. 12. (Color online) Measured amplitude transmission of the array-on-silicon samples made from Ag, Al, and Pb. For clarity, the spectra of Al and Pb arrays are moved down by 0.3 and 0.6, respectively. The vertical dashed line indicates the calculated $[\pm 1, 0]$ metal-Si SP mode at 0.55 THz. The inset shows the corresponding transmittance.

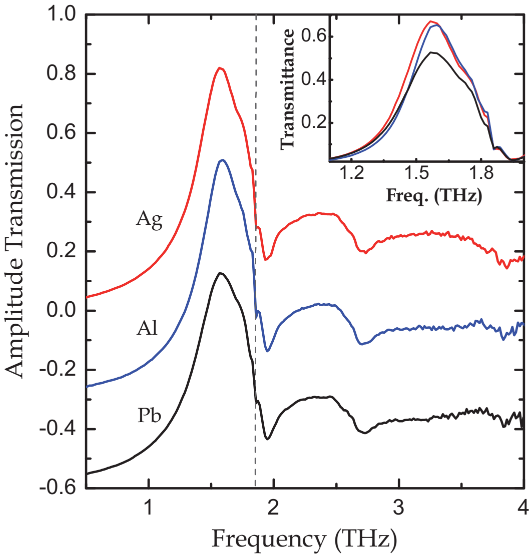

Fig. 13. (Color online) Measured amplitude transmission of the freestanding metal arrays made from Ag, Al, and Pb. For clarity, the spectra of Al and Pb arrays are moved down by 0.3 and 0.6, respectively. The vertical dashed line indicates the calculated $[\pm 1, 0]$ metal-air SP mode. The corresponding transmittance is shown in the inset.

arrays. With metal thicknesses of one-third and three times of skin-depth, the comparison of peak transmittance for these metals remains the same trend as observed with one skin-depth thickness, demonstrating the consistency of our measurements.

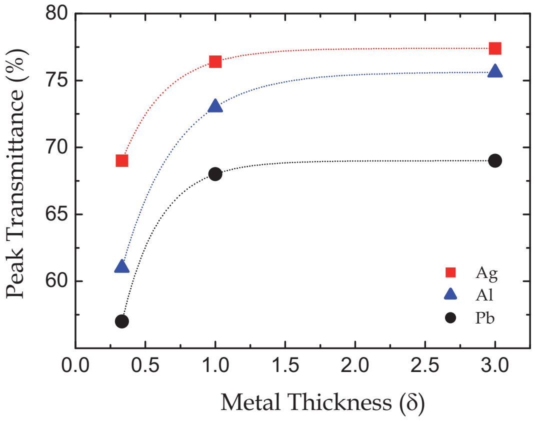

Fig. 14. (Color online) Peak transmittance at the 0.55 $[\pm 1, 0]$ THz metal-Si SP mode for arrays made from Ag, Al, and Pb with different metal thicknesses. The dotted curves are to guide the eye.

The difference in resonant transmission for arrays made from different metals is primarily arisen from the difference in effective propagation length of SPs determined primarily by internal damping and radiation and scattering damping [3]. At terahertz frequencies, the imaginary propagation vector along the metal-dielectric interface approximately given as $k_i = \mathbf{k}_0 \varepsilon_d^{3/2}/(2\varepsilon_{im})$ [10] governs the internal damping, where $\mathbf{k}_0$ is the wave vector of electromagnetic wave in vacuum. Figure 15 shows the calculated k_i for SP resonances along both the metal-Si and the metal-air interfaces. The measured transmission of the metal arrays indeed decreases with increasing k_i. On rough metal surface, besides the internal absorption, radiation and scattering damping also modify the propagation length [4]. As a result, the effective propagation lengths for different metals can be extensively reduced, leading to the difference in the resonant transmission.

4.4 Coupling between SPs and nonresonant transmission

So far, SPs excited at the surface of 2D hole arrays have been considered as a dominant mechanism in extraordinary transmission of electromagnetic waves [1,4]. The recent studies, however, have revealed that besides SPs, localized waveguide resonances or localized modes also make contributions to the extraordinary transmission of light in periodic subwavelength holes [41–43]. To better understand the transmission enhancement mechanism in the terahertz regime, we have studied hole width-dependent terahertz transmission. A characteristic evolution, including well-regulated change in transmittance, linewidth broadening, and blueshift of peak transmission frequencies with respect to hole width were experimentally observed [35]. Based on numerical analysis by the Fano model, we found that terahertz transmission in the 2D hole arrays were associated with two types of contributions, resonant excitation of SPs and nonresonant transmission (or non-SP transmission). The nonresonant transmission exhibited angle-independent peak frequencies and can be resulted from localized effects and direct transmission [22,29,35,41–43]. The localized effects,

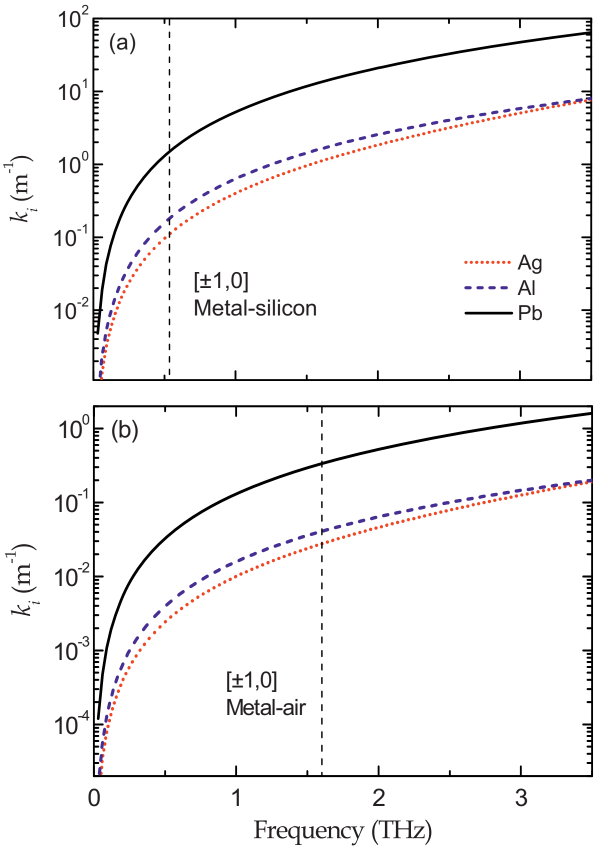

Fig. 15. (Color online) Calculated imaginary propagation vectors of SPs for Ag, Al, and Pb along (a) metal-Si interface and (b) metal-air interfaces.

as either localized modes or localized waveguide resonances [41–43], also contributed substantially to enhanced terahertz transmission. The direct transmission, on the other hand, due to scattering and low filling fraction of metal, was the origin that causes the reduction in transmission efficiency of the holes.

In sample preparation, a set of 2D hexagonal arrays of rectangular subwavelength holes are lithographically fabricated with a 180-nm-thick Al film onto a silicon substrate [35]. Each sample, with dimensions of 15 × 15 mm^2, has holes of a fixed length 120 μm and various widths from 40 to 140 μm with a 20-μm interval, and a constant periodicity of 160 μm. Figure 16 illustrates the frequency-dependent absolute transmittance and the corresponding phase change for an array with hole dimensions of 120 × 40 μm^2. At normal incidence, the resonant frequency can be approximately given by equation (3) with the grating momentum wave vector, $\mathbf{G}_{mn} = 4\pi(m^2+n^2+mn)^{1/2}/\sqrt{3}L$ for the 2D hexagonal hole arrays. The calculated fundamental SP $[\pm1,0]$ resonance of hexagonal arrays at the Al-Si interface was around 0.63 THz, which was higher than the measured transmission peak 0.49 THz due to the fact that the latter was a result of both resonant and nonresonant contributions [10,12,44].

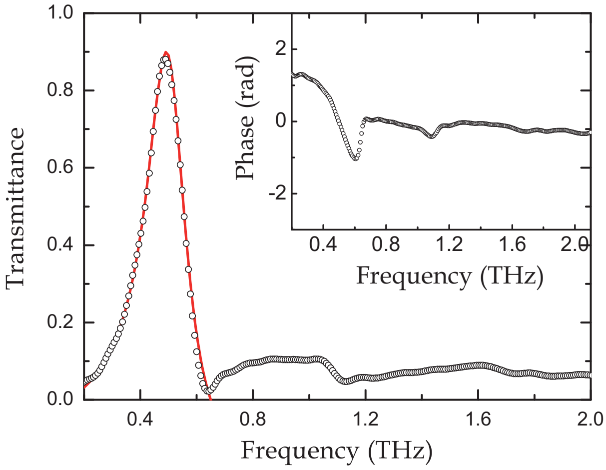

Fig. 16. (Color online) Measured (open circles) and the Fano fit (solid curve) of frequency-dependent transmittance. The fitting parameters are: $q_v = 26.5 \pm 0.2$, $\omega_v/2\pi = 0.49 \pm 0.05$ THz, $\Gamma_v/2\pi = 0.16 \pm 0.01$ THz, and $T_b = (1.28 \pm 0.1) \times 10^{-3}$ for the $[\pm1,0]$ mode. Inset: corresponding data of phase change.

The experimental transmittance was further analyzed by the Fano model, in which the transmission line shape of the arrays was considered as a result of two scattering processes: one refers to the continuum direct scattering state as non-resonant transmission, and the other is the discrete resonant state as SPs [29,44–48]. For an isolated resonance, the Fano model can be written as

$$T_{fano}(\omega) = \left|\tilde{t}(\omega)\right|^2 = T_a + T_b\frac{(\varepsilon_v + q_v)^2}{1+\varepsilon_\nu^2}, \qquad (6)$$

where $\varepsilon_v = (\omega - \omega_v)/(\Gamma_v/2)$, T_a is a slowly varying transmittance, and $|T_b|$ is a coefficient that describes the contribution of a zero-order continuum state coupled to the discrete resonant state. The resonant state is characterized by the resonance frequency ω_v, the linewidth Γ_v, and the Breit-Wigner-Fano coupling coefficient q_v [29,44–48]. The Fano model provided a consistent fit to the measured transmittance as shown in Figure 16, with a peak transmission at $\omega_v/2\pi = 0.49$ THz and a linewidth $\Gamma_v/2\pi = 0.16$ THz.

To better understand the coupling mechanism between SPs and nonresonant transmission, we have studied the set of arrays with various hole widths from 40 to 140 μm. The measured transmittance revealed a hole width dependent evolution, as shown in Figure 17a. An optimal hole width exists, here was 80 μm, with which the peak absolute transmittance T_P approaches the maximum value as depicted in Figure 17b. Meanwhile, the resonance frequency and the corresponding linewidth exhibited monotonic changes. As described in the Fano model, the total transmission is determined by the resonant and non-resonant states and the coupling between them. The all-out transmission probability can be obtained by solving the Hamiltonian, $\hat{H} = \hat{H}_{SP} + \hat{H}_{NRT} + \hat{H}_{Coupling}$. Hence, the coupling can be evaluated by diagonalizing the

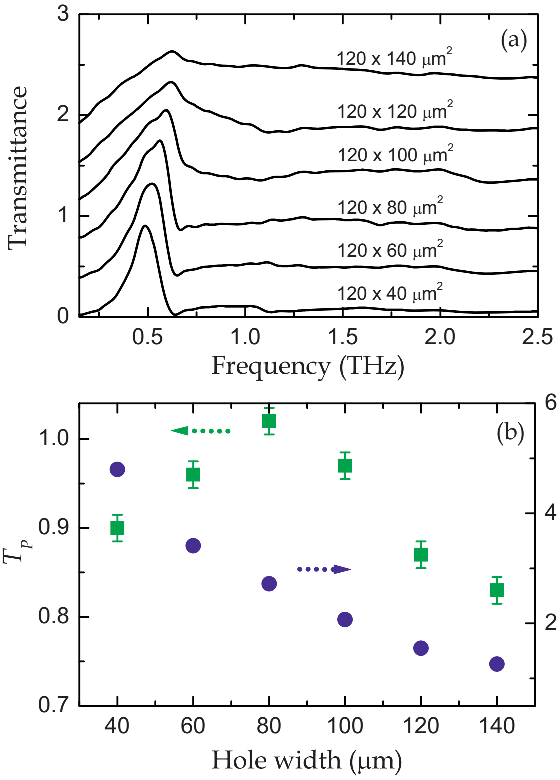

Fig. 17. (Color online) (a) Measured frequency dependent absolute transmittance of the hole arrays with fixed hole length of 120 μm and various hole widths from 40 to 140 μm with an interval of 20 μm. For clarity, the curves are vertically displaced by 0.36. (b) Absolute (squares) and normalized (circles) peak transmittance as a function of hole width.

Hamiltonian matrix [17,35,44,45],

$$H = \hbar \begin{pmatrix} \omega_{SP} & \chi \\ \chi^* & \omega_{NRT} \end{pmatrix}, \tag{7}$$

where ω_{SP} is the resonance frequency of the SP mode given based on the momentum relationship, ω_{NRT} is the frequency of non-resonant transmission, and χ is the coupling coefficient between SPs and non-resonant transmission. Based on the angle-dependent transmission measurements for each array of different hole widths, the coupling $|\chi|^2$ at each angle of incidence can be solved [35].

Figure 18 shows the calculated coupling strength between the SP mode and nonresonant transmission for arrays with different hole widths at normal incidence. With increasing hole width the coupling strength shows monotonic change; it is enhanced from $|\chi|^2 = 1.22 \times 10^{-3}$ at 40 μm to $|\chi|^2 = 6.21 \times 10^{-3}$ at 140 μm. This further explains the measured characteristic evolution in the transmission spectra of these arrays. The increase in hole width, that corresponded to reduced aspect ratio of holes and lower filling fraction of metal, not only led to increased direct transmission through the holes, but also enhanced the coupling between SPs and non-resonant transmission. This in turn gave rise to an increased damping of SPs and thus the linewidth broadened and shifted to higher frequencies towards the peak of nonresonant transmission [29,41,44,49]. Another evidence of the effect of direct transmission due to increased hole width was that T_N, the normalized peak transmittance by the area of holes, exhibited monotonic decrease with hole width, as shown in Figure 17b.

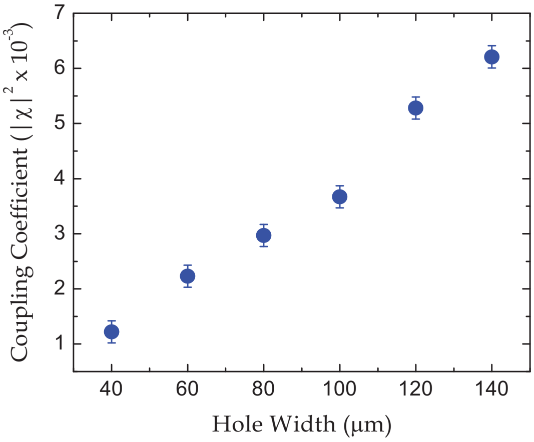

Fig. 18. (Color online) Calculated coupling coefficient of the Al-Si SP $[\pm 1, 0]$ mode with nonresonant transmission for different hole widths at normal incidence.

The maximum absolute peak transmittance T_P achieved at hole width 80 μm (aspect ratio 3:2, filling fraction of metal 62.5%) indicated that the negative effect of direct transmission became critical and challengeed the dominant role of SPs and localized effects when the hole width was further increased. The contributions of localized effects and direct transmission to the effect of non-resonant terahertz transmission may vary with various hole width or aspect ratio and filling fraction of metal. For arrays with filling fraction of metal less than 80%, direct transmission contributed substantially to nonresonant transmission and caused a monotonic decline in normalized transition efficiency.

4.5 Dielectric overlayer effect

One of the fascinating properties of the plasmonic arrays is that their resonant frequencies are extremely sensitive to dielectric function of the medium adjacent to the metal surface. This has made such arrays very promising in biochemical sensing applications [50–52]. In particular, arrays with asymmetric metal-dielectric interfaces on both sides, such as an air-metal-substrate system, provide improved sensitivity because the analytes ($\varepsilon > 1$) applied on the array not only replace air as a dielectric medium at the metal surface, but also easily fill up the hole cavities against the substrate. This in turn provides extensive modification of the SP resonance strength and peak frequencies of the array. By use of THz-TDS, we have investigated effect of a dielectric layer on terahertz transmission through a subwavelength hole array of asymmetric metal-dielectric interfaces [36]. Significant modifications of resonant transmission at the SP modes were observed due to additions of a dielectric overlayer. The metal-air SP $[\pm 1, 0]$ mode at 1.95 THz exhibited up to 0.80 THz remarkable tuning range, while the peak amplitude transmission of the metal-Si SP $[\pm 1, 0]$ mode at 0.5 THz was enhanced from 0.82 to 0.94, owing to resulted change in wave vectors of the SP modes. The experimental results were analyzed by angle-resolved measurements and a frequency domain finite element method (FEM) simulation.

A dielectric layer made from photoresist ($\varepsilon_2 = 2.2 \pm 0.1$ at 1.1 THz, Futurrex, Inc.) was spin-coated on a 180 nm thick Al hole-array-on-Si sample by a single-wafer spin processor (Laurell WS-400A). The array was comprised of 80 μm (x axis) × 100 μm (y axis)-sized rectangular holes with a periodicity of 160 μm. The extracted frequency-dependent amplitude transmission of the array with a dielectric overlayer of various thicknesses d, from 0 to 293 μm, is illustrated in Figure 19a. As indicated by the arrows, the SP resonance of the Al-air $[\pm 1, 0]$ mode shifted remarkably to lower frequencies with increasing d. Without the dielectric layer, the resonance of the Al-air $[\pm 1, 0]$ mode occured at 1.95 THz; while it shifted to 1.87 THz with a layer thickness of 10.3 μm. When the thickness of dielectric layer was increased to 65 μm, this resonance redshifted significantly to 1.25 THz. Further increase in layer thickness, however, led to a little variation at this resonance mode, and it was eventually saturated at 1.17 THz with layer thicknesses varying from 173 to 293 μm. At the resonance frequency of the Al-Si $[\pm 1, 0]$ mode, only minor redshifts was observed due to the overlayer effect, however, the peak amplitude transmission was essentially enhanced with increasing overlayer thickness.

The overlayer resulted resonance shift at the Al-air $[\pm 1, 0]$ SP mode can be understood through the dispersion relation of the SP modes at normal incidence [4,37,38],

$$\mathbf{k}_{sp} = \frac{\omega}{c} \mathrm{Re} \left(\frac{\varepsilon_d \varepsilon_m}{\varepsilon_d + \varepsilon_m} \right)^{1/2}. \tag{8}$$

In this case, without the dielectric layer, the adjacent medium is air, giving $\varepsilon_d = \varepsilon_1 = 1$. When the dielectric film was applied on metal surface and if the film thickness $d > \lambda$ was fulfilled, with λ the resonance wavelength, the dispersion in equation (8) can be modified from $\mathbf{k}_{sp}(\varepsilon_d = \varepsilon_1)$ to $\mathbf{k}_{sp}(\varepsilon_d = \varepsilon_2)$, where ε_2 is the dielectric function of the overlayer film, as shown in the inset of Figure 19b. Thus, the resonant frequency shifted due to modification of the dielectric function of the adjacent medium. When the overlayer thickness was less than the resonance wavelength $d < \lambda$, however, the dielectric layer ε_2 along with the ambient air ε_1 served as an effective adjacent medium to the metal. The shift in SP resonance was arisen from the modification of SP wave vector due to thickness change of the overlayer [53].

In the terahertz regime, since the values of dielectric function of metals are several orders higher than those of dielectric media, $\varepsilon_m = \varepsilon_{Al} \gg \varepsilon_2$, the modified wave vector of SPs due to existence of the dielectric overlayer

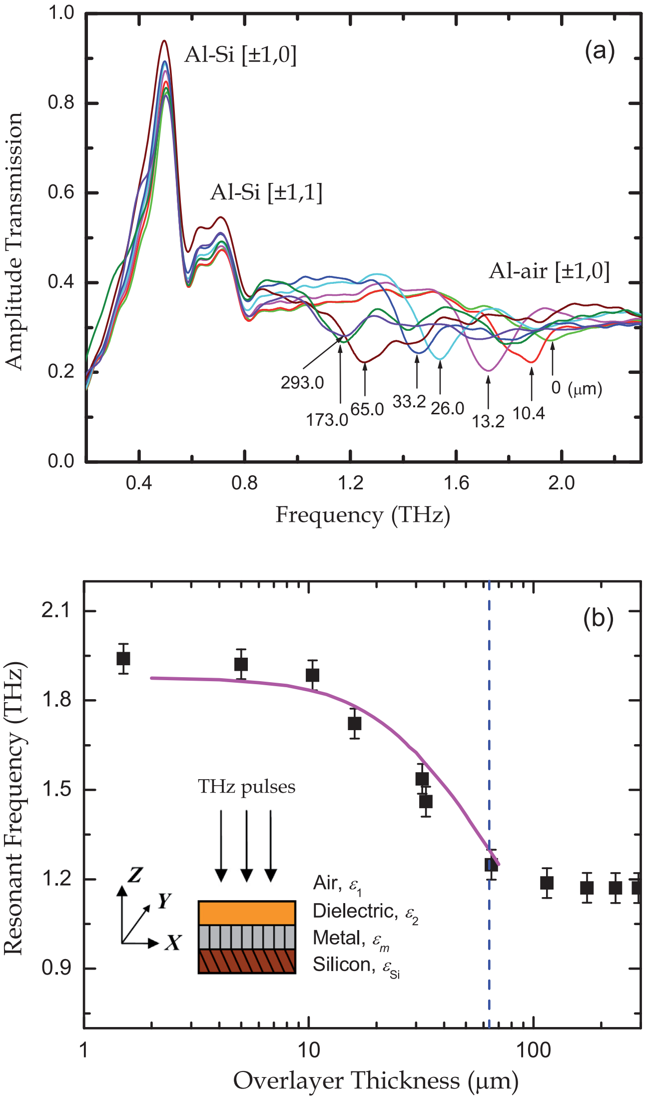

Fig. 19. (Color online) (a) Amplitude transmission of terahertz pulses in the Al hole array with a dielectric overlayer of different thicknesses varying from 0 to 293 μm. (b) Resonance frequencies of the Al-air $[\pm 1, 0]$ SP mode as a function of the thickness of the overlayer dielectric film. Experimental data: squares, numerical calculation: solid curve. Inset: schematic diagram of the array sample.

can approximately given as

$$\mathbf{k}_{sp} \approx \frac{\omega}{c} \left\{ 1 + \left[\frac{1}{2} \left(\frac{\varepsilon_2 - 1}{\varepsilon_2} \right)^2 \right] s^2 \right\}. \tag{9}$$

where $s = \omega d / c$ and c is the light speed [53]. Thus, by combining equations (1) and (9), the SP resonant frequency at the Al-air $[\pm 1, 0]$ mode as a function of the overlayer thickness was calculated, as shown by the solid curve in Figure 19b. Being consistent with the measured results, the theoretical values of the resonant frequency dropped rapidly with increasing film thickness up to 65 μm. Beyond 65 μm, however, the calculated resonant frequency showed a discrepancy with the measured data. This was

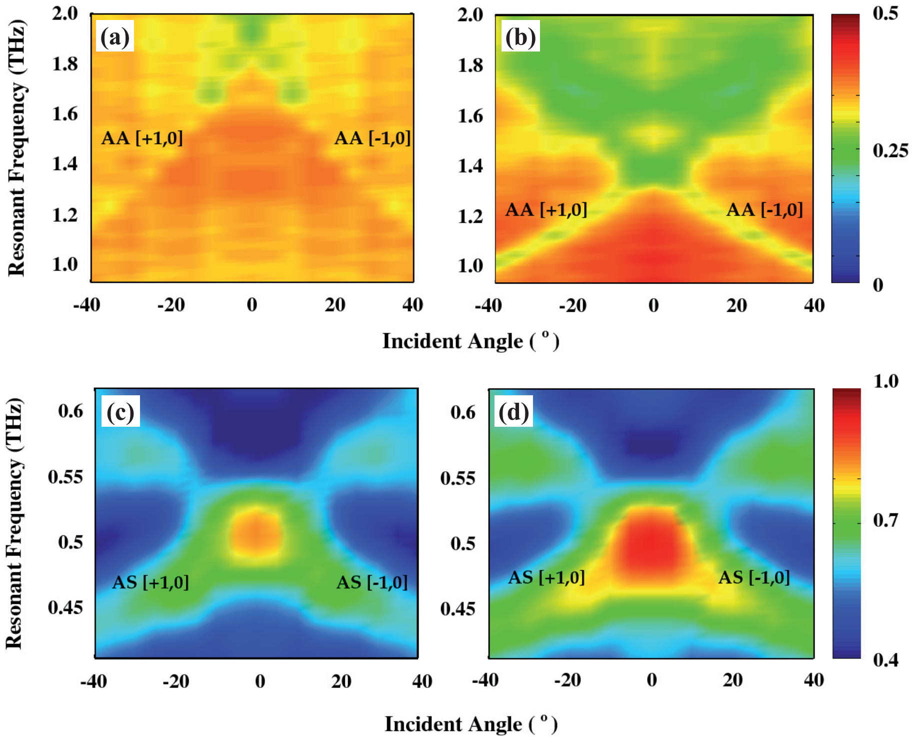

Fig. 20. (Color online) Angle-resolved transmission of the Al-air (AA) $[\pm 1, 0]$ mode without (a) and with (b) the 65 μm-thick dielectric overlayer, and angle-resolved transmission of the Al-Si (AS) $[\pm 1, 0]$ mode without (c) and with (d) the 65 μm-thick dielectric overlayer.

due to the existence of a critical dielectric film thickness, $d_c = \lambda/4(\varepsilon_2 - 1)^{1/2}$; at 1.1 THz, $d_c \approx 63$ μm [53]. When the film thickness $d > d_c$, equation (9) was no more valid, and the resonant frequency showed slow variation with film thickness and eventually approached a constant. In this case, the SP resonance can be evaluated solely at the Al-dielectric layer (ε_2) interface through the relation $\mathbf{k}_{sp} = (\omega/c)\varepsilon_2^{1/2}$ [10].

An angle-resolved transmission measurement was carried to reveal a full band structure of the plasmonic array with and without the overlayer effect at the SP modes. The in-plane wave vector $\mathbf{k}_{||}$ shown in equation (1) is a component of the incident wave vector k_0 in the array plane, defined as $\mathbf{k}_{||} = (\omega/c)\sin\theta$, where θ is incidence angle. Hence, the resonant frequency of the SP mode can be tuned by varying the angle of incidence. Figures 20a and 20b illustrate the full band structures of the Al-air $[\pm 1, 0]$ SP mode without and with the 65 μm-thick dielectric overlayer, respectively, with the incidence angle varied from $-40°$ to $40°$. The amplitude transmission is plotted in the (f, θ) plane with a color scale proportional to the magnitude. The influence of the overlayer on SP resonance properties is clearly observed. The full band of the Al-air $[\pm 1, 0]$ SP mode was shifted towards lower frequencies when the 65 μm-thick dielectric layer was applied on the array surface. It is also of interest to note that the amplitude transmission at the Al-air $[\pm 1, 0]$ SP mode revealed only a minor change with the overlayer thickness, with a minimum around a level of 0.25. This is because that the dielectric layer is nearly transparent at terahertz frequencies and the damping term in this layer can be negligible ($\varepsilon_2'' = 0$) [4,38,54].

While the dielectric film led to a redshift in the SP band at the Al-air SP mode, it also showed a quite distinct influence on the fundamental SP resonance mode at the Al-Si interface. As shown in Figure 19a, the presence of the dielectric layer gave rise to an enhancement in resonant transmission at the Al-Si 0.5 $[\pm 1, 0]$ THz mode [36]. With the 65 μm-thick overlayer, the peak amplitude transmission increased from 0.82 to 0.94 at normal incidence, but it rarely affected the resonant frequency. The full band structure of the Al-Si $[\pm 1, 0]$ mode with the overlalyer remained nearly unchanged compared to that of the bare metal array, except for the increase in transmission strength, as shown in Figures 20c and 20d. This is because that the resonant frequency of SPs at the Al-Si interface was directly related to the dispersion relation described by equation (8) with $\varepsilon_d = \varepsilon_{Si}$, the dielectric function of silicon substrate, and the dielectric function of the overlayer did not make a direct contribution to the resonant frequency of the Al-Si $[\pm 1, 0]$ mode. However, the modification of resonance amplitude with the dielectric layer is interesting. The observed increase in resonant transmission at the Al-Si $[\pm 1, 0]$ mode suggested that there existed an enhanced electric field at the interface due to the presence of the 65 μm-thick dielectric layer.

The field distribution at the array interfaces was modeled to further verify the experimental results [36]. At 0.5 THz, the peak resonance of the Al-Si $[\pm 1, 0]$ mode, the

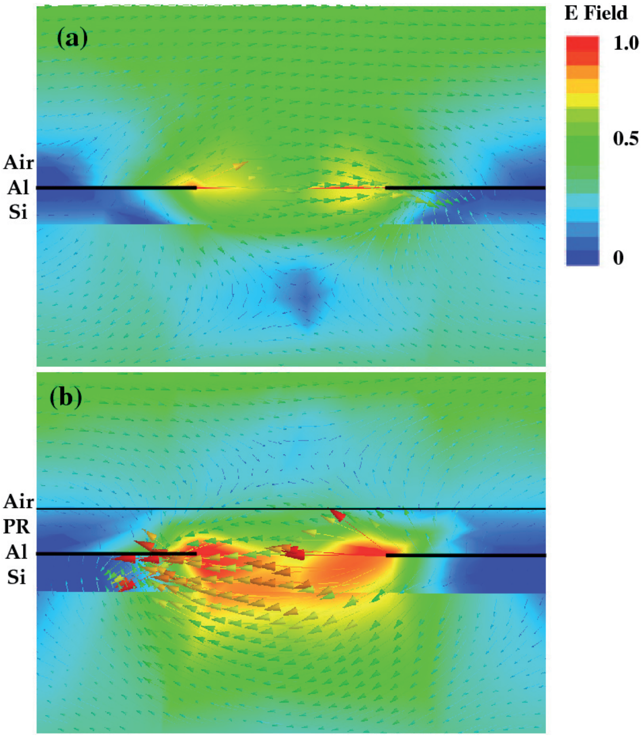

Fig. 21. (Color online) Comparison of modeled electric field by FEM at 0.5 THz, the Al-Si (AS) $[\pm 1, 0]$ mode, without (a) and with (b) the 65 μm-thick dielectric overlayer.

electric field vector is simulated using frequency domain FEM for normal incidence, as illustrated in Figures 21a and 21b, respectively, without and with the 65 μm-thick overlayer. The arrows point at the direction of terahertz electric field $\mathbf{E}$ and the colors are proportional to the magnitude of electric field. The field-line loops were enhanced noticeably into the hole due to addition of the dielectric layer as compared to that of the bare array. The appropriate dielectric overlayer of $\varepsilon_2 > \varepsilon_1$ indeed resulted in the increased coupling of terahertz radiation into SPs at the Dielectric-Al $(\varepsilon_2 - \varepsilon_m)$ interface.

5 Resonant terahertz transmission in semiconductor arrays

In this section, we present our recent work on transmission properties of terahertz radiation in semiconductor plasmonic arrays made from both intrinsically doped and photo-doped silicon thin slabs. An array of elliptical holes made from highly n-doped silicon film has enabled a 175% transmittance when it was normalized to the areas occupied by the holes [27]. More interestingly, in a similar array made from lightly doped silicon, a characteristic evolution of a terahertz SP resonance was observed under variable optical excitations [29]. The SP resonance was developed from an out-of-plane photonics crystal resonance when the real part of dielectric function of the array was switched from positive to negative due to increased photogenerated free carriers.

5.1 Resonant terahertz transmission in highly-doped silicon arrays

Resonant terahertz transmission of an array of subwavelength holes patterned on ultrathin, highly doped silicon was recently investigated. The zero-order transmission spectra exhibited well-defined maxima and minima, as attributed to the resonant excitation of SPs and Wood's anomaly, respectively [4,55]. Transmission anisotropy was investigated in terms of orientation of the elliptical hole array. It was observed that the transmission increased significantly when the major axis of the elliptical hole was perpendicular to the polarization of the terahertz radiation. The measured peak transmittance revealed a 175% efficiency when normalized by the void areas in the holes [27]. In addition, a red-shift and reduction in transmission amplitude were observed when the surrounding dielectric permittivity was increased.

The silicon array, as shown in Figure 4b, was processed from a commercially available n-type, 50-μm-thick silicon wafer with a resistivity of 2×10^{-3} Ωcm and a corresponding high carrier concentration of 3×10^{19} cm^{-3}. The carrier density and the thickness of the doped silicon were chosen to ensure that no terahertz transmission was observed through the unstructured silicon slab. In fact, the corresponding amplitude absorption length was less than 1 μm at 1 THz.

At normal incidence, the resonant frequency of SPs of a square array made from metallic semiconductors can be described by equation (2). Here, $\varepsilon_m = \varepsilon_{rm} + i\varepsilon_{im}$ represents the complex dielectric function constant of the metallic silicon that can be calculated using the simple Drude model [22,56]. At 1.0 THz, with given n-type carrier density, 3×10^{19} cm^{-3} and a corresponding electron mobility, 120 cm^2/Vs [57], the real and imaginary dielectric constants are $\varepsilon_{rm} = -103$ and $\varepsilon_{im} = 1020$, respectively. The ratio $-\varepsilon_{rm}/\varepsilon_{im} = 0.10$ is compatible with that in Al [10], indicating the possibility of resonant excitation of SPs in the silicon array at terahertz frequencies.

The frequency dependent amplitude transmission spectra for both array orientations, $E||x$ and $E||y$, were characterized, as shown in Figure 22a. For the case of $E||x$, the transmission spectrum showed a pronounced peak at 1.6 THz, well below the cutoff, which was 2.0 THz as determined by the 75-μm-sized holes [11,26]. The peak of the transmission magnitude was due to the resonance of SPs and can be attributed to the $[\pm 1, 0]$ SP mode as indicated by a dashed line. We observed a 42% amplitude transmission for the $[\pm 1, 0]$ mode at the silicon-air interface, which led to a power transmission efficiency of 175% when normalized by the voided areas of the holes. In contrast, the resonance peak of the SP $[0, \pm 1]$ mode for the $E||y$ orientation was located at 1.8 THz and showed an amplitude transmission efficiency of 16%. Similar effect of hole structure on terahertz transmission was demonstrated in reference [10], where a higher transmission magnitude was observed for a rectangular hole array than that of a circular holes with the same fundamental periodicity.

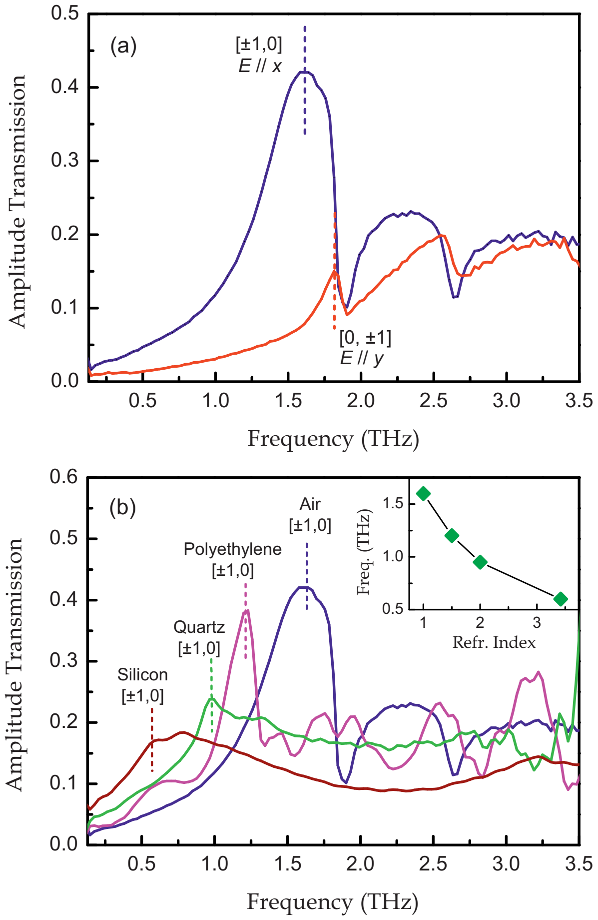

Fig. 22. (Color online) (a) Transmission amplitude spectra of terahertz pulses though the array in different orientations: the major axis perpendicular to the terahertz polarization and the major axis parallel to the terahertz polarization. The dashed lines represent the resonance peaks. (b) Comparison of transmission spectra for different dielectric-array interfaces: air-array-air, polyethylene-array-polyethylene, quartz-array-quartz and silicon-array-silicon. The dashed lines represent the $[\pm 1, 0]$ resonance peaks. Inset: measured resonance frequencies of the $[\pm 1, 0]$ SP modes as a function of the surrounding refractive index.

In both orientations, the transmission resonances of the SP $[0, \pm 1]$ and SP $[\pm 1, 0]$ modes were found well below the cutoff frequency of the holes [11,26]. The minima shown in Figure 22a were identified as the result of Wood's anomaly observed in diffraction grating structures [55]. Wood's anomaly minima occur when a diffracted order becomes tangent to the plane of grating. For a square lattice and normal incidence the wavelengths of Wood's anomaly minima can be approximately given by [58]

$$\omega_{Wood}^{m,n} = c\,\mathbf{G}_{mn}\,\varepsilon_d^{-1/2}. \tag{10}$$

The two calculated Wood's anomaly minima are located at 1.875 $[\pm 1, 0]$ or $[0, \pm 1]$ and 2.652 $[\pm 1, \pm 1]$ THz, respectively, for the silicon-air interface. Clearly, the observed minima in the transmission spectra are well described by equation (10). When the surrounding dielectric constant $\varepsilon_d \ll \varepsilon_m$, the resonant frequency for SPs given in equation (2) may overlap with the frequency of Wood's anomaly minima.

The dependence of SP-assisted transmission properties on the dielectric function of surrounding media were investigated by measuring the zero order transmission through sandwiches made of the array and the desired materials. Four different interfaces were characterized including air-array-air, polyethylene-array-polyethylene, quartz-array-quartz, and silicon-array-silicon [27]. The quartz and polyethylene are fused quartz and low-density polyethylene, respectively. The surrounding silicon was moderately n-doped with a resistivity of 20 $\Omega\,$cm. These surrounding media were fairly transparent to terahertz radiation and have different refractive indices of 1, 1.51, 1.98 and 3.42, respectively, for Air, polyethylene, quartz and silicon. The same subwavelength-structured sample was used as the array and the resonance peaks in the transmission spectra were confirmed by placing the major axis of the hole perpendicular to the terahertz polarization $(E||x)$. The amplitude transmission spectra for different interfaces are shown in Figure 22b, where the $[\pm 1, 0]$ modes are represented by the dashed lines. The experimental result revealed that with increasing refractive index of the surrounding dielectric media, the peak amplitude decreases while the corresponding resonance peak moves toward the lower frequencies as predicted by equation (2). This result is also consistent with the experimental observation in the optical region [58]. The observed resonant frequencies of the $[\pm 1, 0]$ mode as a function of the surrounding refractive index is plotted in the inset of Figure 22b. The low-index material clearly showed pronounced maxima and minima due to the resonant excitation of SPs and Wood's anomaly, respectively. For high-index material, however, the pronounced maxima were relatively broader because of the merging of consecutive resonance peaks. The Wood's anomaly effect also appeared to be weaker due to overlapping with the resonance peaks.

5.2 Transition of a SP resonance from a photonic crystal effect

SP-enhanced terahertz transmission in highly doped semiconductor gratings was recently demonstrated and the resonance can be effectively modulated to a reduced transmission by optical switching [11,27,59]. It thus stimulated an interesting question, how the SP resonance can be evolutionally developed when the real part of dielectric function of the constituent medium is altered instantaneously from positive, across zero to negative? In an effort to investigate such a question, we observed a characteristic evolution of a SP resonance in a semiconductor subwavelength hole array by use of optical pump-terahertz probe measurements [29].

The array sample was made from lightly doped silicon, a fairly transparent medium to terahertz radiation. Its relatively low carrier density is insufficient to support SP resonances. The experimental result revealed that the

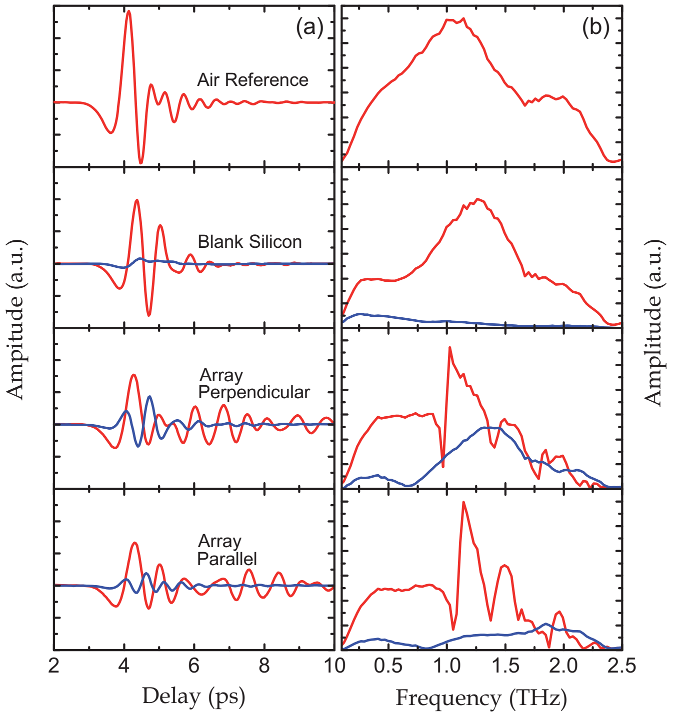

Fig. 23. (Color online) (a) Measured transmitted terahertz pulses and (b) the corresponding Fourier-transformed spectra through air reference, blank Si, Si array of perpendicular, and parallel orientations with (blue curves) and without (red curves) optical excitation of an 111-mW average power.

terahertz transmission properties of the static array were dominated by the out-of-plane two-dimensional photonic crystal effect [60]. When optical excitation was applied to the array, the photo-generated free carriers altered the dielectric properties of Si; the real part of dielectric constant has changed from positive to negative with increasing excitation intensity. As a result, the signature of photonic crystal effect gradually disappeared and SP resonance emerged and was developed into extraordinary terahertz transmission [29].

The array sample was fabricated from commercially available 30-μm-thick n-type Si with 10-Ω cm resistivity and 4×10^{14} cm^{-3} carrier concentration. The sample was a 10 mm × 10 mm-sized array of 80 μm × 40 μm elliptical holes in a square lattice of a periodicity of 160 μm, with structures similar to that shown in Figure 4b. Conventional optical pump-terahertz probe [33] characterization was carried out in an electro-optic terahertz system [34].

Figure 23a illustrates the transmitted teraherz pulses through air reference, blank Si, and the array of both perpendicular and parallel orientations before and after the optical excitation of a 111-mW average power. The perpendicular (parallel) orientation of the array is defined with the longer axis of the elliptical hole perpendicular (parallel) to terahertz electric field. The transmitted terahertz pulse through the unexcited blank Si showed a $\sim$85% amplitude transmission if surface reflections are taken into account. The Si became nearly opaque to terahertz radiation under intense optical excitation due to strong absorption of photo-generated free carriers. The corresponding Fourier-transformed spectra are shown in Figure 23b. In the absence of optical excitation the array can be considered as a two-dimensional out-of-plane photonic crystal slab that has shown complicated spectral structures instead of stopgaps [60]. Under intense optical excitation, however, the transmission spectra exhibited totally different features; the photonic crystal resonances disappeared and SP resonance peaks occured at different frequencies.

The metallic behavior of the array is mainly determined by the negative value of the real dielectric constant $\varepsilon_{rm} < 0$. Under intense optical excitation, the Si array became a complex multilayer medium, composing of a stack of photo-excited Si and unexcited Si layers. At terahertz frequencies, ε_{rm} of the photo-excited layer may turn to negative from being positive under appropriate laser excitation and hence the sample behaved as a metallic array that favored the formation of SPs. The thickness of the photo-excited layer depends on the penetration depth δ_L at the excitation laser wavelength, here $\delta_L = 10$ μm for Si at $\lambda = 800$ nm [37]. In contrast, the penetration depth for terahertz radiation in the photo-excited Si is $\delta_{\mathrm{THz}} = 3.69$ μm at 1.50 THz under 111-mW excitation [4], corresponding to an carrier density $N = 0.99 \times 10^{18}$ cm^{-3}. δ_{THz} can be influenced by laser intensity and it became thinner with increasing optical excitation.

The frequency-dependent terahertz transmission of the array under 111-mW optical excitation for both orientations is plotted in Figure 24a. Transmission enhancement was observed at the fundamental SP 1.50 $[\pm 1, 0]$ THz mode for perpendicular orientation, and 1.85 $[0, \pm 1]$ THz for parallel orientation occurred at the metallic Si-air interface [27]. The orientation-dependent transmission property is consistent with previous work reported in the both visible and terahertz regions [27,61]. In addition, a transmission minimum occurs in the spectra at 1.95 THz due to the Wood's anomaly [16,27,55]. The resonant THz transmission through the photo-induced metallic Si array was analyzed by the typical Fano model, described by equation (6) [46]. As shown in Figure 24a, the Fano fits agree well with the measured fundamental resonances at 111-mW optical excitation [17,44].

To explore the characteristic evolution of the photo-induced SP resonance, the laser excitation was varied from 0 to 111 mW. Figure 24b shows the dependence of complex dielectric constant of the photo-excited Si layer at 1.50 THz, the $[\pm 1, 0]$ SP mode, on laser excitation power. The dielectric function was measured from the reference Si slab where the power absorption α and the refractive index n of the photo-excited Si layer were determined by comparing the transmitted terahertz pulses through the photo-excited and un-excited slab. The dielectric constant was obtained from α and n using the relations $\varepsilon_{rm} = n^2 - k^2$ and $\varepsilon_{im} = 2nk$, where $k = \alpha c/(2\omega)$ [62]. As expected, the real dielectric constant ε_{rm} was evolutionally tuned from positive, across zero to negative with increasing optical power. Above 3 mW, the photo-excited Si layer began to exhibit metallic properties and had a potential to support SPs. Figure 25a illustrates

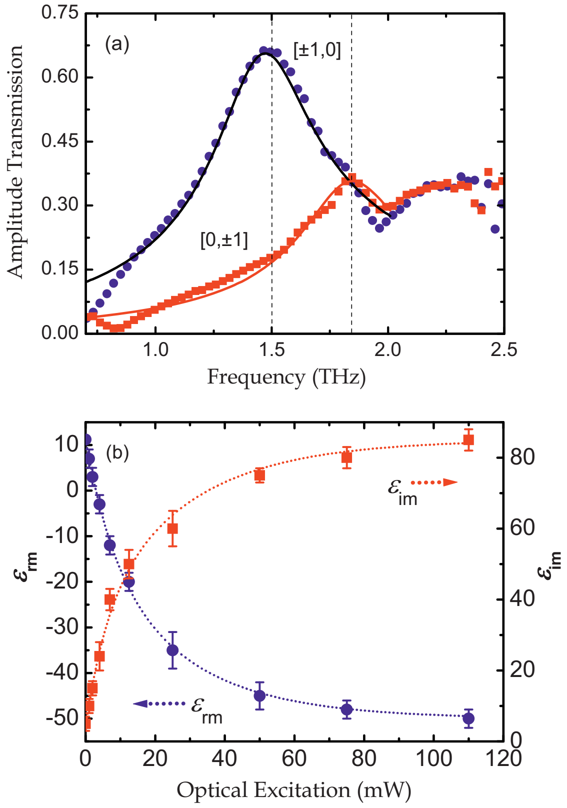

Fig. 24. (Color online) (a) Measured (dots) and the Fano profiles (solid curves) of frequency-dependent terahertz transmission through the Si array in both perpendicular and parallel orientations under 111-mW optical excitation. The vertical dashed lines represent the resonance peaks. The fitting parameters are: $q_v = 12.59 \pm 0.2$, $\omega_v/2\pi = 1.46 \pm 0.05$ THz, $\Gamma_v/2\pi = 0.43 \pm 0.05$ THz, and $T_b = (2.7 \pm 0.1) \times 10^{-3}$ for the $[\pm 1, 0]$ mode; and $q_v = 12.59 \pm 0.2$, $\omega_v/2\pi = 1.81 \pm 0.05$ THz, $\Gamma_v/2\pi = 0.45 \pm 0.05$ THz, and $T_b = (0.8 \pm 0.1) \times 10^{-3}$ for the $[0, \pm 1]$ mode. (b) Measured dielectric function of the photoexcited Si at 1.50 THz as a function of optical excitation. The dotted curves are to guide the eye.

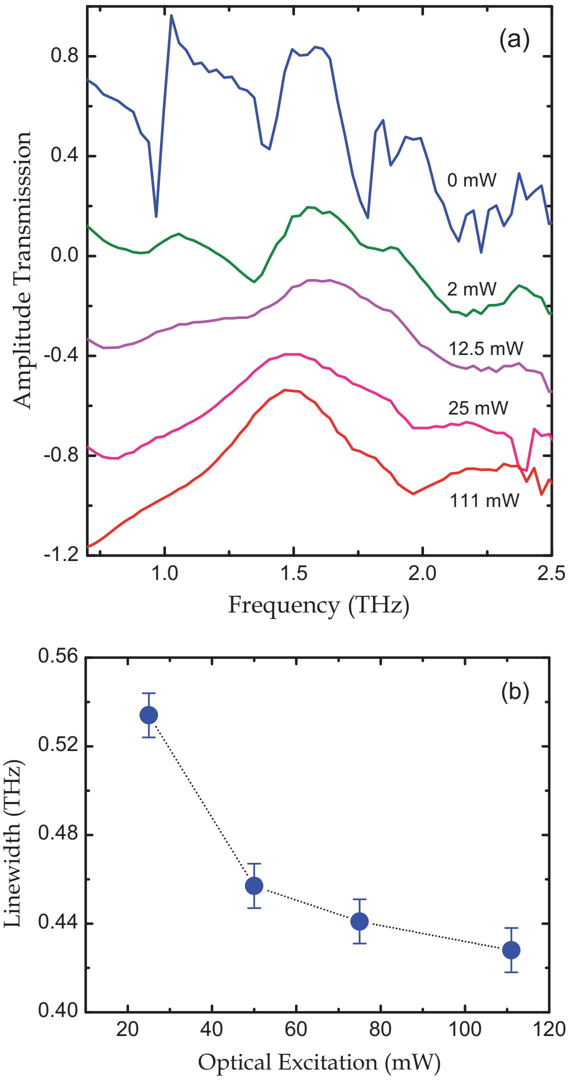

Fig. 25. (Color online) (a) Frequency-dependent terahertz transmission through the array of perpendicular orientation under various laser excitations ranging from 0 to 111 mW. The measurements for different optical excitations are vertically shifted for clarity. (b) Measured resonance linewidth of the SP $[\pm 1, 0]$ mode as a function of optical excitation power. The dotted curve is to guide the eye.

frequency-dependent terahertz transmission through the array of perpendicular orientation under various optical intensities. At low excitation, the transmission was dominated by complex out-of-plane photonic crystal resonances near 0.97, 1.40, and 1.78 THz. When the laser power was increased to 12.5 mW, the photonic crystal effect nearly disappeared; a new resonance peak occurs at 1.60 THz due to the excitation of SPs. The further increase in excitation power gave rise to an enhanced terahertz transmission and a red-shift of resonance peak to 1.50 THz.

The transmission efficiency at the SP resonance 1.50 THz was found to increase with increasing power of laser excitation. At 25 mW, the maximum terahertz transmittance was 25.5%, while it was increased to 45% at 111-mW, corresponding to a 340% transmittance when normalized to the areas of the holes. From the pump-dependent dielectric function shown in Figure 24b, this phenomenon can be understood that the photo-excited Si layer showed improved metallic properties with increasing optical excitation and hence favors the establishment of SPs [20].

It is worth noting when optical excitation was increased above 12.5 mW, narrowing of resonance linewidth occured as shown in Figure 25b, indicating that the damping of SPs becomes less intense. Generally, the total damping of SPs is described by $\Gamma = \Gamma_1 + \Gamma_2$, where Γ_1 is internal damping due to loss at metallic surface and Γ_2 is radiative damping associated mainly with hole size [4,35]. At various optical excitations, the effective size of holes is skin-depth dependent, $d_{eff} = d_0 + 2\delta_{\mathrm{THz}}$, with d_0 the nominal hole width [59]. In our case, the effective hole width is reduced from 48.7 to 47.4 μm with increasing excitations from 25 to 111 mW. Such a slight variation in hole width will not cause obvious change in Γ_2.

This also is confirmed by the resonance frequency that exhibits no shift under excitations above 25 mW [59]. Therefore, the excitation dependent linewidth reduction was mainly originated from the change in Γ_1; the improved metallic properties with increasing optical excitation enabled SPs to be well pronounced [20].

6 Conclusion

Transmission properties of terahertz radiation in 2D plasmonic array of subwavelength holes were investigated. Conventional photolithographic processes were used to pattern the arrays in both metals and semiconductors. Extraordinary terahertz transmission in such arrays was characterized by various terahertz spectroscopy transmission measurements. The frequency-dependent resonant transmission in the 2D hole arrays is understood as a consequence of the resonance excitation of SPs at the metal-dielectric interface. We demonstrated the effect of hole shape, hole dimensions, dielectric properties of the metals, polarization dependence, and metal thickness on enhanced terahertz transmission. Rectangular hole shapes were found to show higher resonant transmission when the polarization of the incident terahertz field is perpendicular to the longer axis of the holes. Efficiently enhanced transmission was also observed in optically thin metallic arrays having thickness of one-third of the skin depth. For similar array transmission is higher for the array made from metal having higher electrical conductivity. In addition, the enhanced terahertz transmission was demonstrated in plasmonic arrays made from semiconductors that possess negative values of the real part of dielectric function.

The author thanks A.K. Azad, J. Han, D. Qu, D. Grischkowsky, Y. Zhao, X. Lu, J. Dai, J. Xu, J. Chen, X.-C. Zhang, M. He, and M. Gong for their outstanding contributions and efforts in this work. The author gratefully acknowledges the support of the US National Science Foundation.

References

1. T.W. Ebbesen, H.J. Lezec, H.F. Ghaemi, T. Thio, P.A. Wolff, Nature **391**, 667 (1998)
2. W.L. Barnes, A. Dereux, T.W. Ebbesen, Nature **424**, 824 (2003)
3. R. Gordon, A.G. Brolo, A. McKinnon, A. Rajora, B. Leathem, K.L. Kavanagh, Phys. Rev. Lett. **92**, 037401 (2004)
4. H. Raether, *Surface plasmons on smooth and rough surfaces and on gratings* (Springer-Verlag, Berlin, 1988), Chap. 2, p. 4
5. E. Ozbay, Science **311**, 189 (2006)
6. W. Srituravanich, N. Fang, C. Sun, Q. Luo, X. Zhang, Nano Lett. **4**, 1085 (2004)
7. X. Luo, T. Ishihara, Appl. Phys. Lett. **84**, 4780 (2004)
8. Z. Liu, Q.H. Wei, X. Zhang, Nano Lett. **5**, 957 (2005)
9. A.V. Zayas, J. Elliott, I.I. Smolyaninov, C.C. Davis, Appl. Phys. Lett. **86**, 151114 (2005)
10. D. Qu, D. Grischkowsky, W. Zhang, Opt. Lett. **29**, 896 (2004)
11. C. Janke, J.G. Rivas, C. Schotsch, L. Beckmann, P.H. Bolivar, H. Kurz, Phys. Rev. B **69**, 205314 (2004)
12. H. Cao, A. Nahata, Opt. Expr. **12**, 1004 (2004)
13. F. Miyamaru, M. Hangyo, Appl. Phys. Lett. **84**, 2742 (2004)
14. J. O'Hara, R.D. Averitt, A.J. Taylor, Opt. Expr. **12**, 6397 (2004)
15. D. Qu, D. Grischkowsky, Phys. Rev. Lett. **93**, 196804 (2004)
16. G. Torosyan, C. Rau, B. Pradarutti, R. Beigang, Appl. Phys. Lett. **85**, 3372 (2004)
17. J.B. Masson, G. Gallot, Phys. Rev. B **73**, 121401 (2006)
18. J.W. Lee, M.A. Seo, D.J. Park, D.S. Kim, S.C. Jeoung, C. Lienau, Q.H. Park, P.C.M. Planken, Opt. Expr. **14**, 1253 (2006)
19. A. Agrawal, T. Matsui, Z.V. Vardeny, A. Nahata, J. Opt. Soc. Am. B **24**, 2545 (2007)
20. T. Thio, H.F. Ghaemi, H.J. Lezec, P.A. Wolff, T.W. Ebbesen, J. Opt. Soc. Am. B **16**, 1743 (1999)
21. D.E. Grupp, H.J. Lezec, T.W. Ebbesen, K.M. Pellerin, T. Thio, Appl. Phys. Lett. **77**, 1569 (2000)
22. M.A. Ordal, L.L. Long, R.J. Bell, S.E. Bell, R.R. Bell, R.W. Alexander Jr., C.A. Ward, Appl. Opt. **22**, 1099 (1983)
23. L. Martín-Moreno, F.J. García-Vidal, H.J. Lezec, A. Degiron, T.W. Ebbesen, Phys. Rev. Lett. **90**, 167401 (2003)
24. A.K. Azad, W. Zhang, Opt. Lett. **30**, 2945 (2005)
25. A.K. Azad, M. He, Y. Zhao, W. Zhang, Opt. Lett. **31**, 2637 (2006)
26. J. Gómez Rivas, C. Schotsch, P. Haring Bolivar, H. Kurz, Phys. Rev. B **68**, 201306 (2003)
27. A.K. Azad, Y. Zhao, W. Zhang, Appl. Phys. Lett. **86**, 141102 (2005)
28. J.G. Rivas, C. Janke, P. Bolivar, H. Kurz, Opt. Expr. **13**, 847 (2005)
29. W. Zhang, A.K. Azad, J. Han, J. Xu, J. Chen, X.-C. Zhang, Phys. Rev. Lett. **98**, 183901 (2007)
30. E. Hendry, F.J. Garcia-Vidal, L. Martin-Moreno, J.G. Rivas, M. Bonn, A.P. Hibbins, M.J. Lockyear, Phys. Rev. Lett. **100**, 123901 (2008)
31. D. Grischkowsky, S. Keiding, M. Van Exter, Ch. Fattinger, J. Opt. Soc. Am. B **7**, 2006 (1990)
32. M. He, A.K. Azad, S. Ye, W. Zhang, Opt. Commun. **259**, 389 (2006)
33. B.I. Greene, J.F. Federici, D.R. Dykaar, A.F.J. Levi, L. Pfeiffer, Opt. Lett. **16**, 48 (1991)
34. B. Ferguson, X.-C. Zhang, Nat. Mater. **1**, 26 (2002)
35. J. Han, A.K. Azad, M. Gong, X. Lu, W. Zhang, Appl. Phys. Lett. **91**, 071122 (2007)
36. J. Han, X. Lu, W. Zhang, J. Appl. Phys. **103**, 033108 (2008)
37. H.F. Ghaemi, T. Thio, D.E. Grupp, T.W. Ebbesen, H.J. Lezec, Phys. Rev. B **58**, 6779 (1998)
38. V.M. Agranovich, D.L. Mills, *Surface Polaritons* (North-Holland, New York, 1982)
39. H.J. Lezec, T. Thio, Opt. Expr. **12**, 3629 (2004)
40. S. Ramo, J.R. Whinnery, *Fields and waves in Modern Radio* (Wiley, New York, 1953), Chap. 6, p. 239

41. K. Molen, K. Koerkamp, S. Enoch, F. Segerink, N. Kulst, L. Kuipers, Phys. Rev. B **72**, 045421 (2005)
42. Z. Ruan, M. Qiu, Phys. Rev. Lett. **96**, 233901 (2006)
43. A. Degiron, T.W. Ebbesen, J. Opt. A: Pure Appl. Opt. **7**, S90 (2005)
44. W. Fan, S. Zhang, B. Minhas, K.J. Malloy, S.R.J. Brueck, Phys. Rev. Lett. **94**, 033902 (2005)
45. C. Genet, M.P. Van Exter, J.P. Woerdman, Opt. Commun. **225**, 331 (2003)
46. U. Fano, Phys. Rev. **124**, 1866 (1961)
47. M. Sarrazin, J. Vigneron, J. Vigoureux, Phys. Rev. B **67**, 085415 (2003)
48. S.H. Chang, S.K. Gray, G.C. Schatz, Opt. Expr. **13**, 3150 (2005)
49. F.J. García de Abajo, J. Sáenz, I. Campillo, J. Dolado, Opt. Expr. **14**, 7 (2006)
50. A.G. Brolo, R. Gordon, B. Leathem, K.K. Kavanagh, Langmuir **20**, 4813 (2004)
51. J. Dintinger, S. Klein, F. Bustos, W.L. Barnes, T.W. Ebbesen, Phys. Rev. B **71**, 035424 (2005)
52. S.M. Williams, K.R. Rodriguez, S. Teeters-Kennedy, A.D. Stafford, S.R. Bishop, U.K. Lincoln, J.V. Coe, J. Phys. Chem. B **108**, 11833 (2004)
53. Z. Schlesinger, A.J. Sievers, Phys. Rev. B **26**, 6444 (1982)
54. G.J. Kovacs, G.D. Scott, Phys. Rev. B **16**, 1297 (1977)
55. R.W. Wood, Phys. Rev. **48**, 928 (1935)
56. M. van Exter, D. Grischkowsky, Appl. Phys. Lett. **56**, 1694 (1990)
57. T.-I. Jeon, D. Grischkowsky, Phys. Rev. Lett. **78**, 1106 (1997)
58. T. Kim, T. Thio, T. Ebbesen, D. Grupp, H. Lezec, Opt. Lett. **24**, 256 (1999)
59. C. Janke, J.G. Rivas, P.H. Bolivar, H. Kurz, Opt. Lett. **30**, 2357 (2005)
60. Z. Jian, D. Mittleman, Appl. Phys. Lett. **87**, 191113 (2005)
61. R. Gordon, M. Hughes, B. Leathem, K.L. Kavanagh, A.G. Brolo, Nano Lett. **5**, 1243 (2005)
62. M.C. Beard, G.M. Turner, C.A. Schmuttenmear, Phys. Rev. B **62**, 15764 (2000)

To access this journal online:
www.edpsciences.org